

A cosmological full-shape power spectra analysis using pre- and post-reconstructed density fields

Weibing Zhang^{1,2}, Ruiyang Zhao^{1,2,3}, Xiaoyong Mu^{1,2}, Kazuya Koyama³, Ryuichi Takahashi⁴, Yuting Wang^{1,5} and Gong-Bo Zhao^{1,2,5}

¹ National Astronomical Observatories, Chinese Academy of Sciences, Beijing, 100101, P.R.China; gbzhao@nao.cas.cn

² School of Astronomy and Space Sciences, University of Chinese Academy of Sciences, Beijing, 100049, P.R.China

³ Institute of Cosmology and Gravitation, University of Portsmouth, Dennis Sciamia Building, Portsmouth PO1 3FX, United Kingdom

⁴ Faculty of Science and Technology, Hirosaki University, 3 Bunkyo-cho, Hirosaki, Aomori 036-8561, Japan

⁵ Institute for Frontiers in Astronomy and Astrophysics, Beijing Normal University, Beijing, 102206, P.R.China

Received 2025 month day; accepted 2025 month day

Abstract In this work, we investigate a joint fitting approach based on theoretical models of power spectra associated with density-field reconstruction. Specifically, we consider the matter auto-power spectra before and after baryon acoustic oscillation (BAO) reconstruction, as well as the cross-power spectrum between the pre- and post-reconstructed density fields. We present redshift-space models for these three power spectra at the one-loop level within the framework of standard perturbation theory (SPT), and perform a joint analysis using three types of power spectra, and quantify their impact on parameter constraints. When restricting the analysis to wavenumbers $k \leq 0.2 h \text{ Mpc}^{-1}$ and adopting a smoothing scale of $R_s = 15 h^{-1} \text{ Mpc}$, we find that incorporating all three power spectra improves parameter constraints by approximately 11%–16% compared to using only the post-reconstruction power spectrum, with the Figure of Merit (FoM) increasing by 10.5%. These results highlight the advantages of leveraging multiple power spectra in BAO reconstruction, ultimately enabling more precise cosmological parameter estimation.

Key words: Cosmic Expansion History — Large-scale-structure — Baryon Acoustic Oscillations — Redshift-space Distortions

1 INTRODUCTION

Large galaxy surveys such as the Dark Energy Spectroscopic Instrument (DESI) (Aghamousa et al. 2016) provide vast datasets that are crucial for exploring cosmic large-scale structure. By extracting key cosmological probes, including baryon acoustic oscillations (BAO) (Eisenstein & Hu 1998; Eisenstein 2005; Cole 2005) and redshift-space distortions (RSD) (Kaiser 1987), these surveys enable tighter constraints on cosmological parameters, offer insights into the nature of dark energy, and provide a powerful framework for testing alternative theories of gravity.

The coupled photon–baryon fluid leaves a signature on the matter distribution after recombination, appearing as a localized peak in the correlation function or an oscillatory pattern in the power spectrum (Eisenstein et al. 1998a; Meiksin et al. 1999). The characteristic scale of BAO serves as a standard ruler for cosmological distance measurements (Eisenstein et al. 1998b). However, nonlinear structure formation driven by gravity broadens and shifts the BAO peak in the correlation function and damps the oscillations in the power spectrum, leading to a loss of phase coherence and the blurring of BAO measurements (Eisenstein et al. 2007b; Smith et al. 2008; Crocce & Scoccimarro 2008; Seo et al. 2008). Nonlinear evolution of BAO is primarily driven by large-scale bulk flows and gravitational clustering, effects that can be partially corrected via standard reconstruction techniques (Eisenstein et al. 2007a). These approaches estimate a displacement field based on the Zel’dovich approximation (Zel’Dovich 1970) and use it to reposition both data and random particles. By separating long-wavelength displacements from the total displacement field, reconstruction effectively transfers crucial information to the reconstructed density field. As a result, standard reconstruction mitigates BAO damping and mode coupling caused by nonlinear evolution, thereby improving measurement precision and reducing systematic shifts (Seo et al. 2008; Padmanabhan et al. 2009; Seo et al. 2010).

Density-field reconstruction in BAO analysis has motivated deeper investigations into its underlying mechanisms for information recovery. During the process of restoring linear modes contaminated by nonlinear effects, reconstruction transfers higher-order statistical information from the unreconstructed density field, δ^{pre} , to the reconstructed density field, δ^{post} (Schmittfull et al. 2015). In the absence of primordial non-Gaussianity, the higher-order N -point statistical information in the pre-reconstruction density field arises from gravitationally driven nonlinear evolution. Since reconstruction acts as an approximate inverse process to this evolution, it reduces the non-Gaussianity of the density field, resulting in a more linear and Gaussian post-reconstruction density field (Hikage et al. 2017, 2020b). Given these properties, density-field reconstruction can be extended beyond BAO analysis to a wide range of topics, including redshift-space distortions (RSD) (Zhu et al. 2018; Hikage et al. 2020a), neutrino properties (Wang et al. 2024b; Zang & Zhu 2024), and primordial non-Gaussianity (Shirasaki et al. 2021; Flöss & Meerburg 2024; Chen et al. 2024).

Although the post-reconstruction power spectrum, P^{post} , retains some of the higher-order information from the original unreconstructed density field beyond what is accessible in the pre-reconstruction power spectrum, P^{pre} , incorporating the cross-power spectrum between the pre- and post-reconstruction fields, P^{cross} , allows for a more comprehensive extraction of cosmological information. Jointly analyzing the three power spectra, referred to as

$$P^{\text{all}} = \{P^{\text{pre}}, P^{\text{post}}, P^{\text{cross}}\},$$

effectively captures higher-order statistical information (Wang et al. 2024b). Density-field reconstruction enables the transformation of higher-order statistics into two-point statistics, allowing P^{post} and P^{cross} to be interpreted in terms of specific higher-order statistics of δ^{pre} (Schmittfull et al. 2015; Wang et al. 2024b; Sugiyama 2024c). Since these three power spectra reflect different levels of nonlinearity, they exhibit distinct dependencies on cosmological parameters and the higher-order statistics of δ^{pre} . A joint analysis of P^{all} therefore helps breaking degeneracies among cosmological parameters and small-scale clustering, substantially improving parameter constraints.

Recently, an emulator-based likelihood analysis using galaxy mocks has further demonstrated the effectiveness of this approach, paving the way for its application to observational survey catalogs (Wang et al. 2024a). Besides emulator-based modeling, perturbation theory (PT) can also be employed for the joint analysis of P^{all} , although modeling smaller scales can be challenging. PT offers valuable insight into the physical underpinnings of this method. Numerous works have developed PT models for the pre-reconstruction power spectrum (Bernardeau et al. 2002), with the effective field theory (EFT) of large-scale structure (Baumann et al. 2012; Ivanov 2022) being widely applied in data analyses (e.g., Ivanov et al. 2020; D’Amico et al. 2020; Zhao et al. 2024; Adame et al. 2024). Furthermore, various studies have proposed PT-based models for P^{post} and P^{cross} (e.g., Padmanabhan et al. 2009; Noh et al. 2009; White 2015; Seo et al. 2016; Hikage et al. 2017; Chen et al. 2019; Sugiyama 2024b; Zhang et al. 2025).

In this paper, we extend the perturbation-theory-based power spectrum framework of Hikage et al. (2020a) by introducing BAO parameters to account for the Alcock–Paczynski (AP) effect (Alcock & Paczynski 1979). We validate our theoretical models for P^{pre} , P^{post} , and P^{cross} using N -body simulation data at redshift $z = 1.02$. The joint analysis of P^{all} yields results consistent with those reported by Wang et al. (2024a).

This paper is organized as follows. Section 2 reviews the theoretical model for the power spectra, Section 3 presents the joint analysis using P^{all} with simulation data, and Section 4 summarizes and discusses our main results.

2 THE MODELING

In this section, we present one-loop models for the pre-, post-reconstruction, and cross-power spectra of the matter density field in redshift space. Our approach is built upon the effective field theory (EFT) of large-scale structure and includes a leading-order counterterm to account for small-scale (UV) physics. We also incorporate parameters associated with the Alcock–Paczynski (AP) effect to properly model geometric distortions.

To describe the power spectrum as an observable, we begin by defining the matter density contrast:

$$\delta(\mathbf{x}) \equiv \frac{\rho(\mathbf{x})}{\bar{\rho}} - 1, \quad (1)$$

where \mathbf{x} is the comoving coordinate, $\rho(\mathbf{x})$ is the local matter density, and $\bar{\rho}$ is the mean density. Under the Newtonian approximation to general relativity, treating matter as a pressureless fluid, the density contrast δ and velocity field \mathbf{v} evolve according to the continuity, Euler, and Poisson equations. Assuming an irrotational velocity field, we introduce the velocity divergence field

$$\theta = \frac{\nabla \cdot \mathbf{v}}{aH}.$$

This set of equations can be solved approximately using standard perturbation theory (SPT). In Fourier space, the n -th order expansions of δ and θ take the form (e.g., Fry 1984; Goroff et al. 1986; Jain & Bertschinger 1994; Scoccimarro & Frieman 1996; Bernardeau et al. 2002):

$$\tilde{\delta}^{(n)}(\mathbf{k}) = D^n(z) \int_{\mathbf{k}=\mathbf{q}_1 \dots \mathbf{q}_n} F_n(\mathbf{q}_1, \dots, \mathbf{q}_n) \tilde{\delta}_L(\mathbf{q}_1) \cdots \tilde{\delta}_L(\mathbf{q}_n), \quad (2)$$

$$\tilde{\theta}^{(n)}(\mathbf{k}) = D^n(z) \int_{\mathbf{k}=\mathbf{q}_1 \dots \mathbf{q}_n} G_n(\mathbf{q}_1, \dots, \mathbf{q}_n) \tilde{\delta}_L(\mathbf{q}_1) \cdots \tilde{\delta}_L(\mathbf{q}_n), \quad (3)$$

where $\mathbf{q}_{1\dots n} = \mathbf{q}_1 + \cdots + \mathbf{q}_n$, $\tilde{\delta}_L$ is the linear density field at $z = 0$, and F_n , G_n are the n -th order perturbation kernels for the matter density and velocity divergence fields, respectively. We adopt the Einstein–de Sitter approximation (Bernardeau et al. 2002), valid in near- Λ CDM cosmologies, so that $D^{(n)}(t) \sim D^n(t)$. For brevity, we write

$$\int_{\mathbf{k}=\mathbf{q}_1 \dots \mathbf{q}_n} \equiv \int \frac{d\mathbf{q}_1 \cdots d\mathbf{q}_n}{(2\pi)^{3n-3}} \delta_D\left(\sum_{j=1}^n \mathbf{q}_j - \mathbf{k}\right), \quad (4)$$

where δ_D is the Dirac delta function.

To account for redshift-space distortions (RSD) under the distant-observer approximation, we relate real- and redshift-space positions according to the conservation condition. The resulting redshift-space density field is (Matsubara 2008b):

$$\tilde{\delta}^z(\mathbf{k}) = \int d\mathbf{x} e^{-i\mathbf{k}\cdot\mathbf{x}} [1 + \delta(\mathbf{x})] e^{-ik_z \frac{v_z(\mathbf{x})}{aH}}, \quad \mathbf{k} \neq \mathbf{0}, \quad (5)$$

where $k_z = \mathbf{k} \cdot \hat{\mathbf{z}} = k\mu$ and $\hat{\mathbf{z}}$ is the unit vector in the line-of-sight direction. Introducing the velocity divergence $\tilde{\theta}(\mathbf{k})$ and expanding the exponential factor $e^{-ik_z \frac{v_z(\mathbf{x})}{aH}}$ in a Taylor series leads to

$$e^{-ik_z \frac{v_z(\mathbf{x})}{aH}} = \sum_{n=0}^{\infty} \frac{(k\mu)^n}{n!} \int \frac{d\mathbf{q}_1 \cdots d\mathbf{q}_n}{(2\pi)^{3n}} \prod_{m=1}^n \frac{\mu_m}{q_m} \tilde{\theta}(\mathbf{q}_m) e^{i\mathbf{q}_m \cdot \mathbf{x}}, \quad (6)$$

where $\mu_m = \mathbf{q}_m \cdot \hat{\mathbf{z}}/q_m$. By substituting Eq. (6) into Eq. (5) and performing a perturbative expansion of the density field δ and velocity divergence field θ , one can derive the n -th order density fluctuation in redshift space as:

$$\tilde{\delta}^{(n)}(\mathbf{k}) = D^n(z) \int_{\mathbf{k}=\mathbf{q}_1 \dots \mathbf{q}_n} Z_n(\mathbf{q}_1, \dots, \mathbf{q}_n) \tilde{\delta}_L(\mathbf{q}_1) \cdots \tilde{\delta}_L(\mathbf{q}_n), \quad (7)$$

where Z_n is the n -th order redshift-space kernel (e.g., Heavens et al. 1998; Scoccimarro et al. 1999; Matsubara 2008a; Hikage et al. 2020a). In what follows, we omit the superscript “z”.

We apply the standard reconstruction technique (Eisenstein et al. 2007a), which estimates a shift field $\tilde{\mathbf{s}}$ from the smoothed nonlinear density field $\tilde{\delta}$ using the negative Zel’dovich approximation (Zel’dovich 1970):

$$\tilde{\mathbf{s}}(\mathbf{k}) = -i \frac{\mathbf{k}}{k^2} W(k) \tilde{\delta}(\mathbf{k}), \quad W(k) = \exp(-k^2 R_s^2/2), \quad (8)$$

with $R_s = 15 h^{-1}$ Mpc. This procedure mitigates nonlinear effects from bulk flows and cluster formation. Displacing both data and random particles by $\tilde{\mathbf{s}}(\mathbf{k})$ yields the displaced and shifted fields $\tilde{\delta}^{(d)}$ and $\tilde{\delta}^{(s)}$, whose difference defines the reconstructed density field:

$$\tilde{\delta}^{(\text{rec})} \equiv \tilde{\delta}^{(d)} - \tilde{\delta}^{(s)}. \quad (9)$$

Because the matter sample has a sufficiently high number density, discreteness effects in reconstruction (Sugiyama 2024c) are negligible.

An analogous perturbative expansion exists for $\tilde{\delta}^{(\text{rec})}$:

$$\tilde{\delta}^{(\text{rec},n)}(\mathbf{k}) = D^n(z) \int_{\mathbf{k}=\mathbf{q}_1 \dots \mathbf{q}_n} Z_n^{(\text{rec})}(\mathbf{q}_1, \dots, \mathbf{q}_n) \tilde{\delta}_L(\mathbf{q}_1) \cdots \tilde{\delta}_L(\mathbf{q}_n), \quad (10)$$

where $Z_n^{(\text{rec})}$ is given by Hikage et al. (2020a,b).

Having obtained perturbative forms for the density fields before and after reconstruction, we can compute the redshift-space power spectrum

$$\langle \tilde{\delta}(\mathbf{k}) \tilde{\delta}(\mathbf{k}') \rangle = (2\pi)^3 \delta_D(\mathbf{k} + \mathbf{k}') P(\mathbf{k}). \quad (11)$$

Up to one-loop order, the pre-reconstruction power spectrum is

$$P_{1\text{-loop}}(k, \mu) = D^2(z) P_{11}(k, \mu) + D^4(z) [P_{22}(k, \mu) + P_{13}(k, \mu)], \quad (12)$$

where

$$P_{11}(k, \mu) = (1 + f\mu^2)^2 P_L(k), \quad (13)$$

$$P_{22}(k, \mu) = 2 \int \frac{d\mathbf{q}}{(2\pi)^3} [Z_2(\mathbf{k} - \mathbf{q}, \mathbf{q})]^2 P_L(|\mathbf{k} - \mathbf{q}|) P_L(q), \quad (14)$$

$$P_{13}(k, \mu) = 6(1 + f\mu^2) P_L(k) \int \frac{d\mathbf{q}}{(2\pi)^3} Z_3(\mathbf{k}, \mathbf{q}, -\mathbf{q}) P_L(q), \quad (15)$$

$P_L(k)$ is the linear power spectrum at $z = 0$, and $f \equiv d \ln D / d \ln a$ is the linear growth rate. Similar expressions hold for the one-loop post-reconstruction power spectrum and the cross-power spectrum, but

the second-order and third-order kernels (Z_2, Z_3) are replaced by their post- and cross-reconstruction counterparts ($Z_2^{(\text{rec})}, Z_3^{(\text{rec})}$) and ($Z_2^{(\text{x})}, Z_3^{(\text{x})}$) (Zhang et al. 2025).

Theoretical predictions are often expanded into Legendre multipoles:

$$P_\ell(k) = \frac{2\ell + 1}{2} \int_{-1}^1 d\mu P(k, \mu) \mathcal{P}_\ell(\mu), \quad (16)$$

where $\mathcal{P}_\ell(\mu)$ is the Legendre polynomial of order ℓ . One-loop SPT alone does not fully capture nonlinear small-scale physics, so EFT introduces a counterterm to absorb UV contributions. For the one-loop pre-reconstruction spectrum, the counterterm is proportional to $k^2 P_L(k)$ (Senatore & Zaldarriaga 2014). We adopt a similar form for the post-reconstruction and cross-power spectra (Hikage et al. 2020a; Zhang et al. 2025):

$$P_{\text{ct},\ell}(k) = c_\ell k^2 P_\ell^L(k). \quad (17)$$

Converting redshift to comoving distance introduces the Alcock–Paczynski (AP) effect (Alcock & Paczynski 1979), which distorts (k, μ) when the fiducial cosmology differs from the true one. Labeling true-cosmology coordinates by (k', μ') , the full power spectrum with counterterms reads

$$P^{\text{theory}}(k', \mu') = P_{\text{1-loop}}(k', \mu') + P_{\text{ct}}(k', \mu'), \quad (18)$$

and we recover the 2D power spectrum from its multipoles for $\ell = 0, 2, 4$. Higher-order multipoles are negligible for the scales of interest. The AP effect rescales k and μ according to

$$k' = \frac{k}{\alpha_\perp} \sqrt{1 + \mu^2(F^{-2} - 1)}, \quad \mu' = \frac{\mu/F}{\sqrt{1 + \mu^2(F^{-2} - 1)}}, \quad F = \frac{\alpha_\parallel}{\alpha_\perp},$$

where

$$\alpha_\parallel = \frac{H^f(z_{\text{eff}}) r_d^f}{H(z_{\text{eff}}) r_d}, \quad \alpha_\perp = \frac{D_A(z_{\text{eff}}) r_d^f}{D_A^f(z_{\text{eff}}) r_d},$$

relate AP parameters to Hubble function H and the angular diameter distance D_A at the effective redshift z_{eff} , and r_d is the sound horizon at the drag epoch. Note that the superscript f indicates fiducial values. Discrete k -binning in measurements is accounted for by averaging the theoretical predictions over each bin:

$$P_\ell^{\text{th}}(k_{\text{bin}}) \approx \frac{\int_{k_{\text{bin},\text{min}}}^{k_{\text{bin},\text{max}}} dk k^2 P_\ell^{\text{AP}}(k)}{\int_{k_{\text{bin},\text{min}}}^{k_{\text{bin},\text{max}}} dk k^2}, \quad (19)$$

where $P_\ell^{\text{AP}}(k)$ includes the AP transformation. This procedure allows a more accurate comparison between theory and binned data $P_\ell^{\text{data}}(k_{\text{bin}})$ in subsequent likelihood analyses.

3 RESULTS

In this section, we present our analysis using a suite of high-resolution N -body simulations. This mock dataset was previously used in Hikage et al. (2020b); Zhang et al. (2025). The input cosmological parameters for these simulations are based on the best-fit values from the Planck 2015 TT, TE, EE+lowP measurements: $\Omega_b = 0.0492$, $\Omega_m = 0.3156$, $h = 0.6727$, $n_s = 0.9645$, and $\sigma_8 = 0.831$ (Ade et al. 2016).

The initial linear power spectrum is computed using CAMB (Lewis et al. 2000), which is also used to calculate our theoretical model predictions. The initial mass particle distribution is generated with second-order Lagrangian perturbation theory (2LPT) (Crocco et al. 2006; Nishimichi et al. 2009). We then perform N -body simulations using Gadget-2 (Springel 2005) to generate 4000 realizations, each

with a box size of $L = 500 h^{-1} \text{Mpc}$, containing 512^3 particles at redshift $z = 1.02$. After standard reconstruction is applied to each realization, the multipoles of the pre-reconstruction, post-reconstruction, and cross-power spectra are measured from the simulation samples. Owing to the large measurement uncertainties associated with the hexadecapole, only monopole and quadrupole measurements are used in this work. Further details on the simulation data and reconstruction procedure can be found in Hikage et al. (2020b).

We measure the power spectrum multipole components from 4000 realizations of our simulations and use them to estimate the covariance matrix:

$$\mathbf{Cov}_{\ell, \ell'}(k, k') = \frac{1}{N-1} \sum_{i=1}^N [P_{\ell, i}(k) - \bar{P}_{\ell}(k)] [P_{\ell', i}(k') - \bar{P}_{\ell'}(k')], \quad (20)$$

where $N = 4000$ is the total number of realizations, and $\bar{P}_{\ell}(k) = \frac{1}{N} \sum_{i=1}^N P_{\ell, i}(k)$ is the mean power spectrum multipole across all realizations.

Due to the limited box size $L = 500 h^{-1} \text{Mpc}$, the mean power spectrum \bar{P}_{ℓ} exhibits a pronounced sawtooth pattern on large scales, especially for $\ell \geq 2$. To mitigate this effect, we use an additional set of 8 realizations with a larger volume, $V = (4 h^{-1} \text{Gpc})^3$, to correct the $V = (500 h^{-1} \text{Mpc})^3$ data following Zhang et al. (2025):

$$\bar{P}_{\ell}^{(T), 4h^{-1} \text{Gpc}} = \frac{\bar{P}_{\ell}^{(\text{pre}), 4h^{-1} \text{Gpc}}}{\bar{P}_{\ell}^{(\text{pre}), 500h^{-1} \text{Mpc}}} \bar{P}_{\ell}^{(T), 500h^{-1} \text{Mpc}}, \quad (21)$$

where $T \in \{\text{pre}, \text{post}, \text{cross}\}$ and the superscripts $4h^{-1} \text{Gpc}$ or $500h^{-1} \text{Mpc}$ indicate the side length of the simulation box. These larger-volume simulations are run with the same cosmological parameters as the $500 h^{-1} \text{Mpc}$ boxes (Hikage et al. 2020b). This ‘‘grid correction’’ ensures an accurate representation of large-scale modes, thereby improving our subsequent likelihood analysis.

The likelihood function is given by

$$\mathcal{L} = \exp\left(-\frac{\chi^2}{2}\right), \quad (22)$$

where the chi-square statistic takes the form

$$\chi^2(\mathbf{p}) = \sum_{\ell, \ell'=0, 2} \sum_{\substack{i, j \\ k_{\min} \leq k_i, k_j \leq k_{\max}}} \left[P_{\ell}^{\text{th}}(k_i; \mathbf{p}) - P_{\ell}^{\text{sim}}(k_i) \right] \mathbf{Cov}_{\ell, \ell'}^{-1}(k_i, k_j) \left[P_{\ell'}^{\text{th}}(k_j; \mathbf{p}) - P_{\ell'}^{\text{sim}}(k_j) \right]. \quad (23)$$

Since the number of realizations N is finite, the inverse of the covariance matrix is rescaled by the Hartlap factor $(N - N_{\text{bin}} - 2)/(N - 1)$ (Hartlap et al. 2007), where N_{bin} is the number of bins used in the fit.

In each power spectrum model, we treat five parameters as free:

$$\mathbf{p} = \{\alpha_{\parallel}, \alpha_{\perp}, f, c_0, c_2\}. \quad (24)$$

In the joint fit using three types of power spectra, the parameters α_{\parallel} , α_{\perp} , and f are shared across all three models, while each model retains its own counterterm parameters (c_0, c_2) . This results in 9 total free parameters. All parameters have uniform (flat) priors, $\mathcal{U}(\min, \max)$, whose ranges are listed in Table 1.

Table 1: Priors for free parameters.

Parameter	α_{\parallel}	α_{\perp}	f	c_0	c_2
Prior	$\mathcal{U}(0.6, 1.4)$	$\mathcal{U}(0.6, 1.4)$	$\mathcal{U}(0.2, 1.5)$	$\mathcal{U}(-10^3, 10^3) h^{-2} \text{Mpc}^2$	$\mathcal{U}(-10^3, 10^3) h^{-2} \text{Mpc}^2$

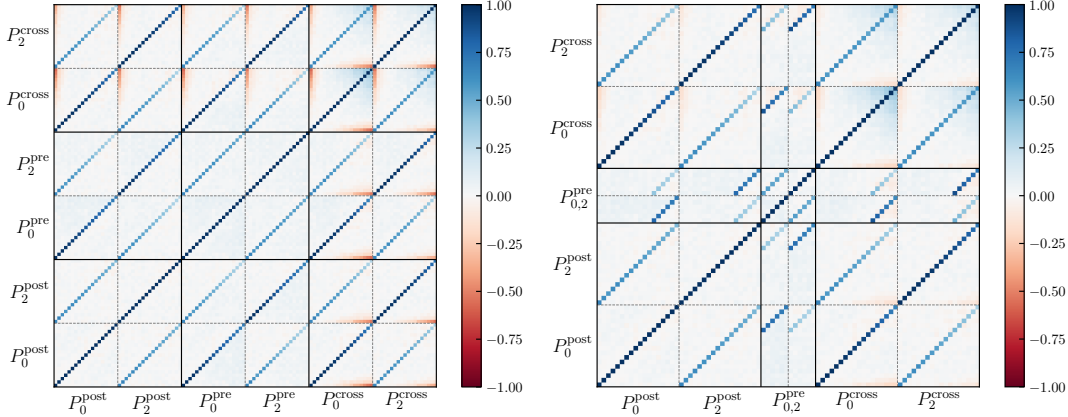


Fig. 1: Correlation coefficient matrices derived from the covariance matrix in Eq. (20). The reconstruction is performed with a smoothing scale $R_s = 15h^{-1} \text{Mpc}$, using modes up to $k_{\text{max}} = 0.20 h \text{Mpc}^{-1}$. *Left panel*: the full matrix, with $k_{\text{min}} = 0.01 h \text{Mpc}^{-1}$ for all three power spectra. *Right panel*: a modified setup where $k_{\text{min}}^{\text{pre}} = 0.14 h \text{Mpc}^{-1}$ and $k_{\text{min}}^{\text{post}} = k_{\text{min}}^{\text{cross}} = 0.02 h \text{Mpc}^{-1}$.

We construct our parameter estimation pipeline within the `Cobaya` framework (Torrado & Lewis 2021), using Markov Chain Monte Carlo (MCMC) sampling (Lewis & Bridle 2002) to explore the posterior distributions. The resulting MCMC chains are analyzed with `GetDist` (Lewis 2019), which yields marginalized posteriors and the corresponding contour plots. To ensure convergence, we require the Gelman–Rubin statistic to satisfy $R-1 < 0.001$. In addition, we use `iminuit` (Dembinski & et al. 2020; James & Roos 1975) to minimize χ^2 and obtain the best-fit parameter values.

Our likelihood analysis includes both individual and joint fits of the three power spectra, using a smoothing scale $R_s = 15h^{-1} \text{Mpc}$. In individual fits, we set $k_{\text{min}} = 0.02 h \text{Mpc}^{-1}$. For our main results, we adopt $k_{\text{max}} = 0.20 h \text{Mpc}^{-1}$, while also testing a more conservative choice of $k_{\text{max}} = 0.16 h \text{Mpc}^{-1}$. The corresponding results for this more conservative limit are presented in Appendix A.

Table 2: Best-fit values, 68% confidence intervals, and Figures of Merit (FoM) for the various fit configurations shown in Fig. 2, assuming $k_{\text{max}} = 0.20 h \text{Mpc}^{-1}$. The last column indicates the relative reduction in parameter uncertainties and the increase in FoM for the joint fit P^{all} compared to the post-reconstruction fit P^{post} . The fiducial values of the parameters are $\alpha_{\parallel}^f = \alpha_{\perp}^f = 1$ and $f_{\text{in}} = 0.8796$.

Case	P^{pre}	P^{post}	P^{cross}	P^{all}	$1 - \sigma^{\text{all}}/\sigma^{\text{post}}$
α_{\parallel}	$1.016_{-0.047}^{+0.035}$	$1.005_{-0.032}^{+0.028}$	$1.006_{-0.034}^{+0.029}$	0.999 ± 0.028	11%
α_{\perp}	0.995 ± 0.082	1.001 ± 0.047	1.003 ± 0.056	0.996 ± 0.040	16%
f	0.89 ± 0.15	0.865 ± 0.084	0.87 ± 0.10	0.832 ± 0.073	14%
FoM	17.3	24.6	22.4	27.2	10.5%

In the joint analysis of $P^{\text{all}} = \{P^{\text{pre}}, P^{\text{post}}, P^{\text{cross}}\}$, we initially attempted a combined fit using all data points with $k \in (0.02, 0.20) h \text{Mpc}^{-1}$. However, because all three power spectra closely resemble the linear power spectrum on large scales, their correlation coefficients (the correlation among P^{pre} , P^{post} and P^{cross} at the same k) approaches unity, as seen in the left panel of Fig. 1. This means that including all three power spectra in the analysis is redundant, which can cause numerical instabilities when we invert the data covariance matrix.

To address this issue, we remove part of the large-scale modes from the pre-reconstruction power spectrum, which effectively reduces the redundancy in the data vector. In practice, we set $k_{\text{min}}^{\text{pre}} =$

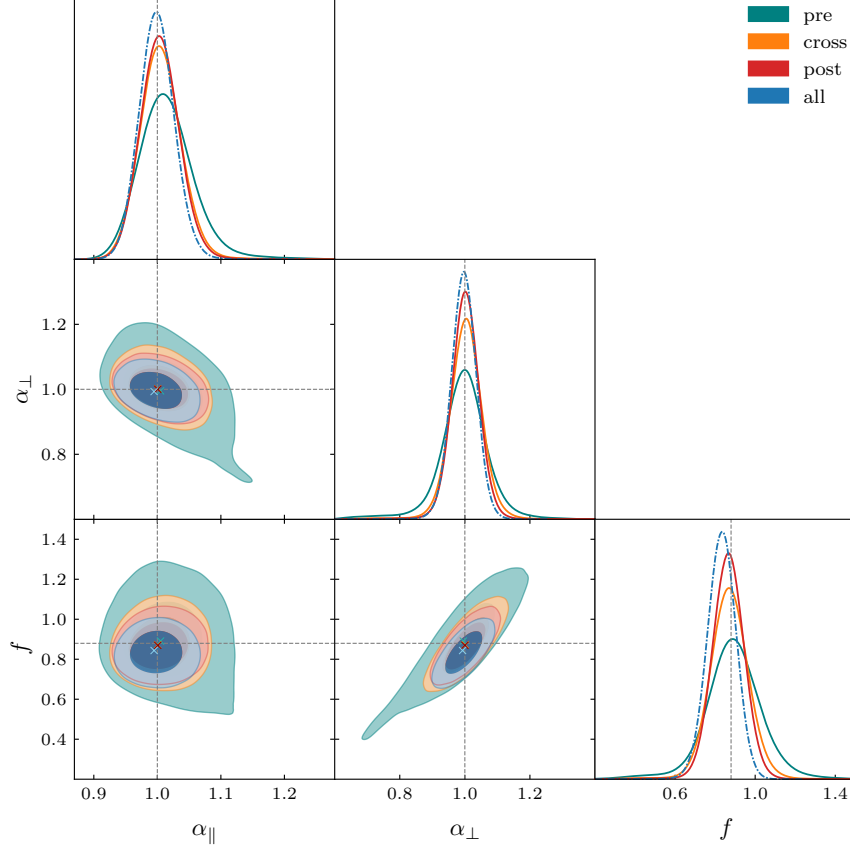


Fig. 2: Constraints on the parameters $\{\alpha_{\parallel}, \alpha_{\perp}, f\}$ obtained by fitting the theoretical model to the monopole and quadrupole of the pre-reconstruction (*teal*), post-reconstruction (*red*), and cross-power (*orange*) spectra, as well as all three simultaneously (*blue*). The crosses mark the best-fit parameters, and the dashed lines show the fiducial values. The reconstruction is performed with $R_s = 15 h^{-1} \text{Mpc}$. In individual fits, the wavenumber range is $0.02 < k < 0.20 h \text{Mpc}^{-1}$. For the joint fit (P^{all}), we choose $k_{\text{min}}^{\text{pre}} = 0.14 h \text{Mpc}^{-1}$ and $k_{\text{min}}^{\text{post,cross}} = 0.02 h \text{Mpc}^{-1}$, with $k_{\text{max}} = 0.20 h \text{Mpc}^{-1}$.

$0.14 h \text{Mpc}^{-1}$ and $k_{\text{min}}^{\text{post}} = k_{\text{min}}^{\text{cross}} = 0.02 h \text{Mpc}^{-1}$. The right panel of Fig. 1 shows the correlation coefficients after this cut, whose absolute values are all well below unity, ensuring a stable numeric inversion in the likelihood analysis.

Figure 2 presents the resulting constraints on BAO and RSD parameters obtained from each individual power spectrum ($P^{\text{pre}}, P^{\text{post}}, P^{\text{cross}}$) and their combined fit P^{all} . The best-fit results are all consistent with the fiducial parameter values within the 68% confidence region. Among the individual fits, P^{post} delivers the tightest constraints, with P^{cross} performing comparably well. A complete summary of these results is provided in Table 2.

Table 2 also demonstrates how the joint fit $P^{\text{all}} = \{P^{\text{pre}}, P^{\text{post}}, P^{\text{cross}}\}$ substantially tightens the parameter constraints relative to the post-reconstruction power spectrum alone, offering reductions in σ_p of up to 14%. The corresponding Figure of Merit (FoM) for the BAO and RSD parameters, defined as

$$\text{FoM} = \left[\frac{1}{\det(\mathbf{C})} \right]^{1/(2N_p)}, \quad (25)$$

also shows a 10.5% enhancement when combining all three power spectra, where \mathbf{C} is the covariance matrix of $\{\alpha_{\parallel}, \alpha_{\perp}, f\}$ estimated from the Markov Chain Monte Carlo (MCMC) samples, and $N_p = 3$ denotes the number of free parameters in \mathbf{C} . This underscores the value of including all available spectra to achieve tighter cosmological parameter constraints.

Using the best-fit parameters obtained from each fit, we compute the corresponding theoretical monopole and quadrupole power spectra and compare them with the simulation data in Fig. 3. We decompose the linear power spectrum into wiggle and no-wiggle components via a polynomial-based method (Hinton et al. 2017), writing $P_L(k) = P_w(k) + P_{\text{nw}}(k)$. Applying the fiducial linear growth rate $f_{\text{in}} = 0.8796$, we calculate the linear redshift-space power spectrum and its multipoles using the Kaiser formula (Kaiser 1987):

$$P^L(k, \mu) = (1 + f_{\text{in}} \mu^2)^2 P_L(k). \quad (26)$$

For ease of comparison, both theoretical and simulation power spectra are divided by $P_{\ell, \text{nw}}$. Figure 3 also shows the corresponding linear monopole and quadrupole; as expected, BAO wiggles become more prominent in the post-reconstruction and cross-power spectra than in the pre-reconstruction spectrum. Meanwhile, the cross-power spectrum exhibits a gradually decreasing amplitude, owing to the absence of IR cancellation (Sugiyama 2024a).

As seen in Fig. 3, the monopole and quadrupole from each individually fitted model agree closely with the simulation data, and the joint fit (P^{all}) also provides consistent results. Notably, for both post-reconstruction and cross-power spectra, the joint-fit curves are similar to those obtained in the individual fits. However, the BAO wiggles in P^{pre} are not perfectly captured by the current perturbation theory approach. Incorporating IR resummation (Sugiyama 2024a,b) could further improve the BAO modeling, and we plan to pursue this extension in future work.

4 CONCLUSION AND DISCUSSIONS

In this paper, we conduct a full-shape analysis for BAO and RSD parameters using the power spectra derived from both pre- and post-reconstruction density fields, while also including their cross-power spectrum. Our theoretical framework is developed at one-loop order in redshift space for the matter density field. We incorporate the Alcock–Paczynski (AP) effect into our models to constrain BAO parameters.

To extend standard perturbation theory (SPT) to smaller scales, we introduce effective field theory (EFT) counterterms to account for unmodeled ultraviolet (UV) physics. However, the counterterms may partially degenerate with infrared (IR) contributions and other modeling uncertainties. Our theoretical models for P^{pre} , P^{post} , and P^{cross} thus fit simulation data for the power spectrum multipoles, constraining the BAO parameters $\alpha_{\parallel}, \alpha_{\perp}$ and the linear growth rate f . Each of these three models provides unbiased parameter estimates individually up to $k_{\text{max}} = 0.2 h \text{ Mpc}^{-1}$, assuming a reconstruction smoothing scale $R_s = 15 h^{-1} \text{ Mpc}$ and a covariance matrix estimated from 4000 N -body realizations at redshift $z = 1.02$, each with a volume of $(500 h^{-1} \text{ Mpc})^3$. Among these models, P^{post} yields the tightest constraints, while P^{cross} is intermediate between P^{pre} and P^{post} , yet quite close to the latter in terms of constraining power.

We carry out a joint fit of all three power spectra, $P^{\text{all}} = \{P^{\text{pre}}, P^{\text{post}}, P^{\text{cross}}\}$, to further tighten parameter constraints. Because these spectra are strongly correlated on large scales, especially P^{pre} and P^{post} , numerical instability in the covariance matrix can arise when using limited-volume simulations and a finite number of realizations. In addition, small-scale nonlinearities may also bias the inferred parameters if not fully captured by the perturbation theory. We employ a pragmatic remedy in this work: increasing the minimum wavenumber k_{min} for P^{pre} to $0.14 h \text{ Mpc}^{-1}$, which significantly reduces the bias in f . We find that raising k_{min} for P^{cross} also yields similar but milder benefits. Ultimately, we opt to remove large-scale modes of P^{pre} alone, given its stronger correlation with P^{post} and its weaker individual constraining power.

With these adjustments, the joint fit P^{all} delivers unbiased best-fit parameter values while improving constraints relative to P^{post} alone, yielding uncertainty reductions of about 11%, 16%, and 14% in α_{\parallel} ,

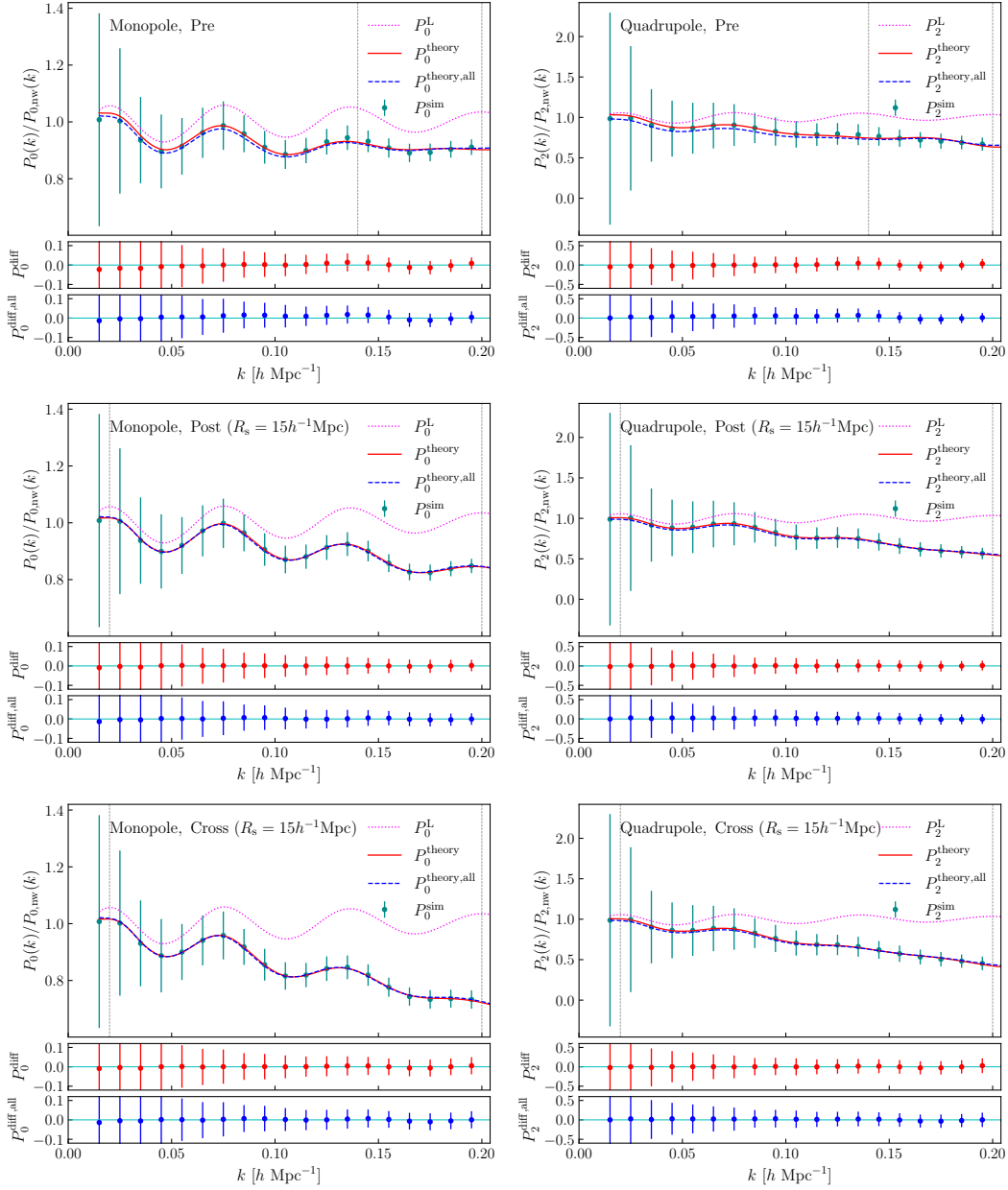


Fig. 3: Comparison of the measured and modeled power spectrum monopole ($\ell = 0$, left column) and quadrupole ($\ell = 2$, right column) for pre-reconstruction (top panels), post-reconstruction (middle panels), and cross-power (bottom panels). The teal points with error bars denote the simulation results and their standard deviations. The red solid curves are the best-fit theoretical predictions from individual fits of each power spectrum, whereas the blue dashed curves display the predictions from the joint fit of all three spectra. The magenta dotted lines show the linear theory power spectra computed from the fiducial cosmology. All power spectra are divided by the corresponding no-wiggle linear reference. The bottom portion of each subplot shows $P_\ell^{\text{diff}} \equiv P_\ell^{\text{sim}}/P_\ell^{\text{theory}} - 1$, the relative difference between the simulations and the theoretical prediction. The vertical gray dashed lines mark the lower and upper k -cuts used in the joint fits.

α_{\perp} , and f , respectively. Additionally, the figure of merit (FoM) for the joint fit is enhanced by 10.5%. These results corroborate earlier findings (Wang et al. 2024b,a) that the three spectra together retain complementary information about the pre-reconstruction density field, enabling greater precision than any individual spectrum can achieve.

We confirm that each power spectrum model separately reproduces the simulation results well, barring some mismatch in the BAO wiggles for P^{pre} . Likewise, the joint analysis accurately recovers both simulation and theoretical predictions.

Looking ahead to applications in real surveys such as DESI, we plan to improve the theoretical model by recognizing the mismatches between assumed and true cosmological parameters for the BAO reconstruction (Sherwin & White 2019), incorporating the IR resummation (Sugiyama 2024a,b), introducing galaxy bias and other observational effects, and evaluating the approach with halo or galaxy catalogs. We also anticipate exploring FFTLog techniques (Hamilton 2000) and theory-based emulators to expedite the computational pipeline.

Acknowledgements We thank Chiaki Hikage for contributions in the early stage of this work. WZ, RZ, XM, YW, and GBZ are supported by the National Natural Science Foundation of China (NSFC) under Grant 11925303. KK is supported by the Science and Technology Facilities Council (STFC) under Grant ST/W001225/1. RT is supported by JSPS KAKENHI grant Nos. JP22H00130 and JP20H05855. YW further acknowledges support from the National Key R&D Program of China No. (2022YFF0503404, 2023YFA1607800, 2023YFA1607803), NSFC Grants (12273048, 12422301), the CAS Project for Young Scientists in Basic Research (No. YSBR-092), and the Youth Innovation Promotion Association CAS. GBZ also acknowledges support from the CAS Project for Young Scientists in Basic Research (No. YSBR-092), the China Manned Space Project, and the New Cornerstone Science Foundation through the XPLOER Prize.

Appendix A: SUPPLEMENTARY TEST RESULTS FOR DIFFERENT SCALE RANGES

In this section, we provide supplementary results that explore how the choice of scale range affects our analysis. Specifically, we consider a more conservative maximum wavenumber of $k_{\text{max}} = 0.16 h \text{ Mpc}^{-1}$, complementing our primary results at $k_{\text{max}} = 0.20 h \text{ Mpc}^{-1}$ in the main text.

Figure A.1 shows the constraints on α_{\parallel} , α_{\perp} , and f obtained from the individual fits of P^{pre} , P^{post} , and P^{cross} , as well as the joint fit P^{all} , at $k_{\text{max}} = 0.16 h \text{ Mpc}^{-1}$. Here, P^{cross} performs similarly to P^{post} . The combined fit P^{all} continues to yield the tightest constraints—particularly on the AP parameters—but offers only a marginal improvement in f compared to P^{post} . This is in contrast to the more substantial gain in f noted in the main text for $k_{\text{max}} = 0.20 h \text{ Mpc}^{-1}$. The detailed results are presented in Table A.1, which also compares the Figure of Merit (FoM) across different scenarios. Specifically, P^{all} reduces the uncertainties in α_{\parallel} , α_{\perp} , and f by 17%, 17%, and 8%, respectively, relative to P^{post} , while increasing the FoM by 8.3%.

Table A.1: Same format as Table 2, but corresponding to Fig. A.1 at $k_{\text{max}} = 0.16 h \text{ Mpc}^{-1}$.

Case	P^{pre}	P^{post}	P^{cross}	P^{all}	$1 - \sigma^{\text{all}}/\sigma^{\text{post}}$
α_{\parallel}	$1.029^{+0.045}_{-0.088}$	$1.011^{+0.048}_{-0.073}$	$1.017^{+0.044}_{-0.073}$	$1.010^{+0.045}_{-0.061}$	17%
α_{\perp}	$0.986^{+0.11}_{-0.092}$	1.00 ± 0.10	$0.995^{+0.086}_{-0.077}$	0.998 ± 0.083	17%
f	$0.86^{+0.19}_{-0.17}$	0.86 ± 0.15	0.85 ± 0.17	0.83 ± 0.14	8%
FoM	12.1	14.4	14.0	15.6	8.3%

In Fig. A.2, we compare the theoretical predictions (using best-fit parameters corresponding to Fig. A.1) against the measured multipoles. We again find good agreement between theory and data for both individual fits and the joint fit P^{all} .

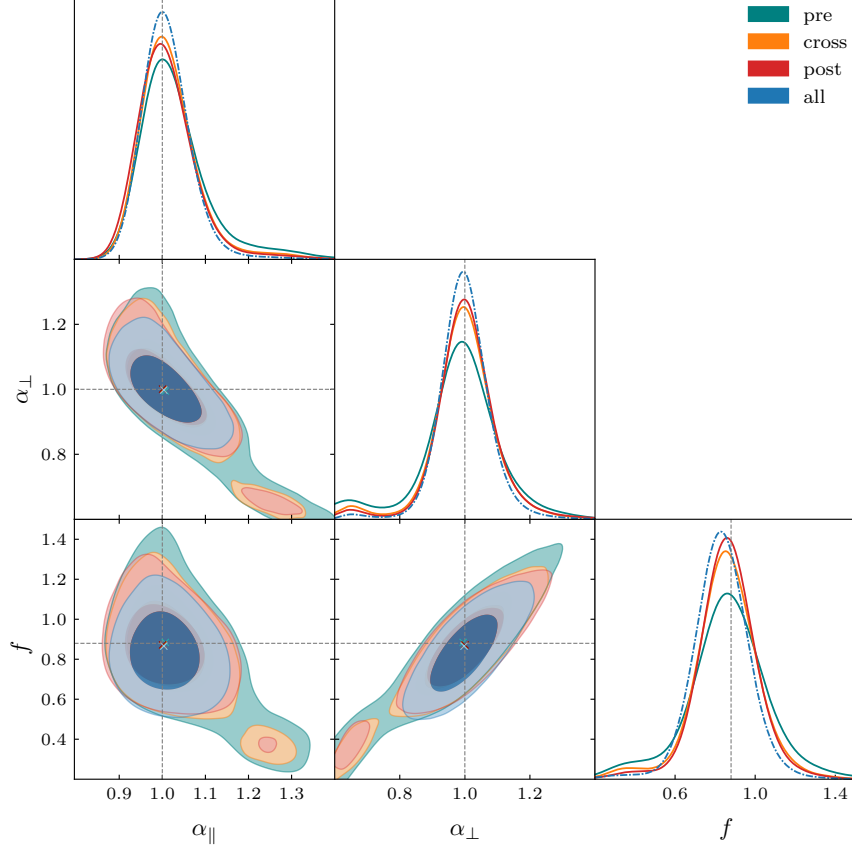


Fig. A.1: Similar to Fig. 2, but with $k_{\max} = 0.16 h \text{ Mpc}^{-1}$.

In Section 3 of the main text, we stressed the importance of cutting large-scale modes to ensure robust joint fits of P^{all} . Here, we expand on that discussion by fixing $k_{\max}^{\text{all}} = 0.20 h \text{ Mpc}^{-1}$ and exploring how varying k_{\min} influences the resulting parameter constraints. As shown in Fig. A.3, taking $k_{\min} = 0.02 h \text{ Mpc}^{-1}$ for all spectra produces a best-fit linear growth rate f that is noticeably smaller than its fiducial value, reflecting the strong correlations among the three power spectra on large scales and the ensuing instability in the inverse covariance matrix. The left panel of Fig. A.3 demonstrates that this bias in f decreases as k_{\min}^{pre} is increased. Similarly, the right panel shows that raising k_{\min}^{cross} , or both k_{\min}^{pre} and k_{\min}^{cross} , mitigates the bias, although to a slightly lesser degree. Based on these tests, in the main text we chose $k_{\min}^{\text{pre}} = 0.14 h \text{ Mpc}^{-1}$ for the joint fits, as this approach most effectively reduces biases while retaining sufficient constraining power.

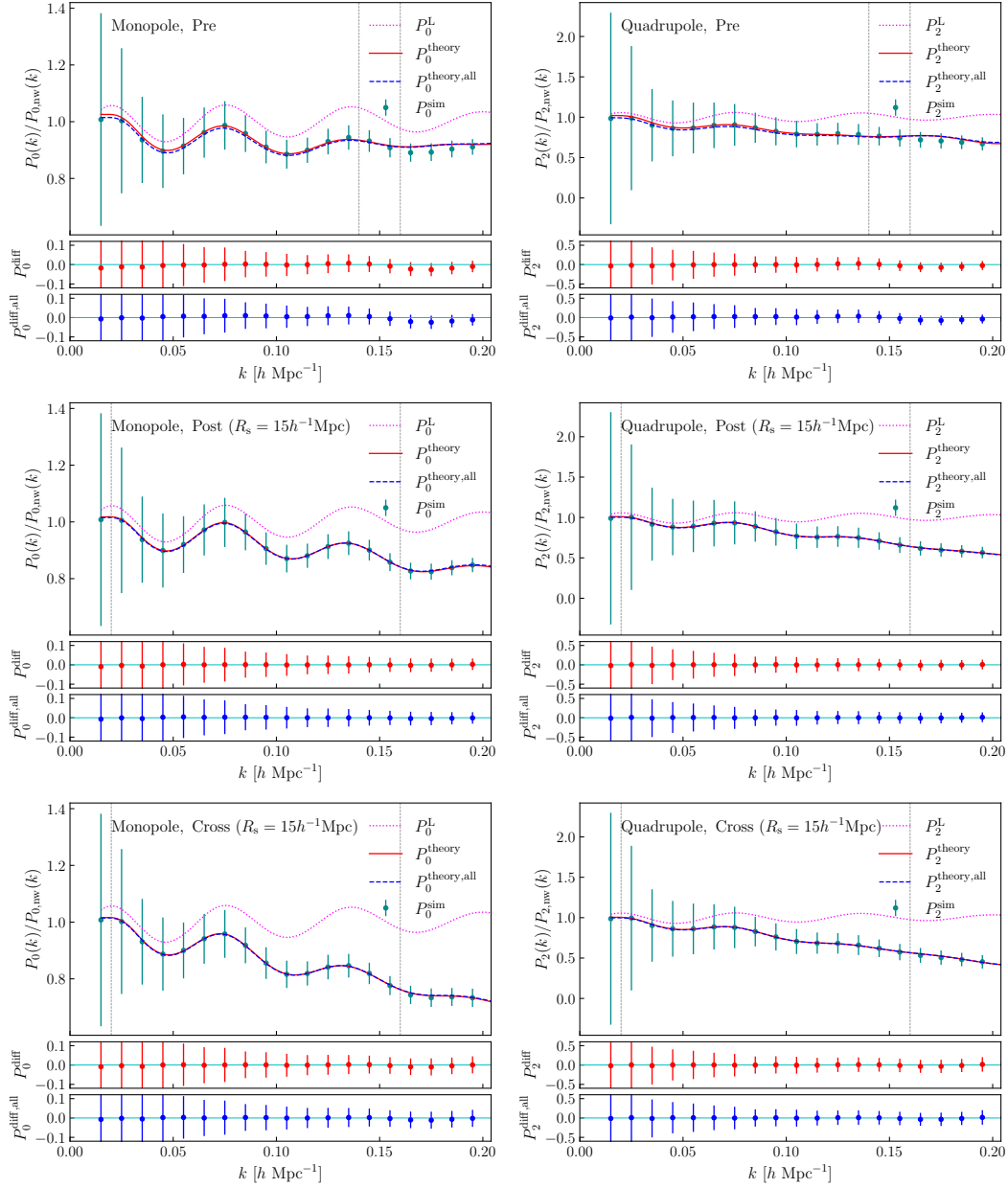


Fig. A.2: Same as Fig. 3, but with $k_{\max} = 0.16 h \text{ Mpc}^{-1}$. Each panel compares the simulation data to theoretical predictions derived from best-fit parameters.

References

- Adame, A. G., et al. 2024, arXiv:2411.12022 2
Ade, P. A. R., et al. 2016, *Astron. Astrophys.*, 594, A13 5
Aghamousa, A., et al. 2016, arXiv:1611.00036 1
Alcock, C., & Paczynski, B. 1979, *Nature*, 281, 358 3, 5
Baumann, D., Nicolis, A., Senatore, L., & Zaldarriaga, M. 2012, *JCAP*, 07, 051 2

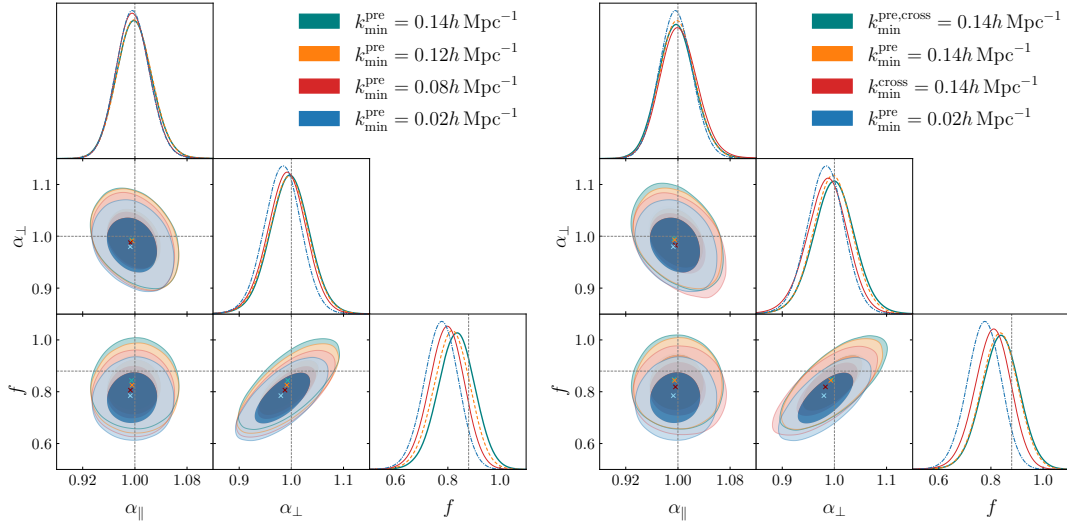


Fig. A.3: Constraints on α_{\parallel} , α_{\perp} , and f from joint fits of P^{all} under different large-scale cuts, with $R_s = 15 h^{-1} \text{Mpc}$ and $k_{\text{max}}^{\text{all}} = 0.20 h \text{Mpc}^{-1}$ held fixed. *Left panel*: varying $k_{\text{min}}^{\text{pre}} = 0.08 h \text{Mpc}^{-1}$ (red), $0.12 h \text{Mpc}^{-1}$ (orange), and $0.14 h \text{Mpc}^{-1}$ (teal), compared to the baseline $k_{\text{min}}^{\text{all}} = 0.02 h \text{Mpc}^{-1}$ (blue). *Right panel*: increasing $k_{\text{min}}^{\text{cross}} = 0.14 h \text{Mpc}^{-1}$ (red), $k_{\text{min}}^{\text{pre}} = 0.14 h \text{Mpc}^{-1}$ (orange), or both simultaneously (teal), again relative to the baseline (blue). Crosses mark the best-fit values for each setup, and gray dashed lines denote the fiducial parameters.

- Bernardeau, F., Colombi, S., Gaztanaga, E., & Scoccimarro, R. 2002, *Phys. Rept.*, 367, 1 2, 3
- Chen, S.-F., Vlah, Z., & White, M. 2019, *JCAP*, 09, 017 2
- Chen, X., Padmanabhan, N., & Eisenstein, D. J. 2024, arXiv:2412.00968 2
- Cole, S. e. a. 2005, *Monthly Notices of the Royal Astronomical Society*, 362, 505 1
- Crocce, M., Pueblas, S., & Scoccimarro, R. 2006, *Mon. Not. Roy. Astron. Soc.*, 373, 369 5
- Crocce, M., & Scoccimarro, R. 2008, *Phys. Rev. D*, 77, 023533 2
- D’Amico, G., Gleyzes, J., Kokron, N., et al. 2020, *JCAP*, 05, 005 2
- Dembinski, H., & et al., P. O. 2020 7
- Eisenstein, D. J. e. a. 2005, *The Astrophysical Journal*, 633, 560 1
- Eisenstein, D. J., & Hu, W. 1998, *The Astrophysical Journal*, 496, 605 1
- Eisenstein, D. J., Hu, W., Silk, J., & Szalay, A. S. 1998a, *Astrophys. J. Lett.*, 494, L1 2
- Eisenstein, D. J., Hu, W., & Tegmark, M. 1998b, *Astrophys. J. Lett.*, 504, L57 2
- Eisenstein, D. J., Seo, H.-j., Sirko, E., & Spergel, D. 2007a, *Astrophys. J.*, 664, 675 2, 4
- Eisenstein, D. J., Seo, H.-j., & White, M. J. 2007b, *Astrophys. J.*, 664, 660 2
- Flöss, T., & Meerburg, P. D. 2024, *JCAP*, 02, 031 2
- Fry, J. N. 1984, *Astrophys. J.*, 279, 499 3
- Goroff, M. H., Grinstein, B., Rey, S. J., & Wise, M. B. 1986, *Astrophys. J.*, 311, 6 3
- Hamilton, A. J. S. 2000, *Mon. Not. Roy. Astron. Soc.*, 312, 257 11
- Hartlap, J., Simon, P., & Schneider, P. 2007, *Astron. Astrophys.*, 464, 399 6
- Heavens, A. F., Matarrese, S., & Verde, L. 1998, *Mon. Not. Roy. Astron. Soc.*, 301, 797 4
- Hikage, C., Koyama, K., & Heavens, A. 2017, *Physical Review D*, 96, 043513 2
- Hikage, C., Koyama, K., & Takahashi, R. 2020a, *Phys. Rev. D*, 101, 043510 2, 3, 4, 5
- Hikage, C., Takahashi, R., & Koyama, K. 2020b, *Phys. Rev. D*, 102, 083514 2, 4, 5, 6
- Hinton, S. R., et al. 2017, *Mon. Not. Roy. Astron. Soc.*, 464, 4807 9
- Ivanov, M. M. 2022, arXiv e-prints, arXiv:2212.08488 2
- Ivanov, M. M., Simonović, M., & Zaldarriaga, M. 2020, *JCAP*, 05, 042 2

- Jain, B., & Bertschinger, E. 1994, *Astrophys. J.*, 431, 495 3
- James, F., & Roos, M. 1975, *Comput. Phys. Commun.*, 10, 343 7
- Kaiser, N. 1987, *Mon. Not. Roy. Astron. Soc.*, 227, 1 1, 9
- Lewis, A. 2019, arXiv:1910.13970 7
- Lewis, A., & Bridle, S. 2002, *Phys. Rev. D*, 66, 103511 7
- Lewis, A., Challinor, A., & Lasenby, A. 2000, *Astrophys. J.*, 538, 473 5
- Matsubara, T. 2008a, *Physical Review D*, 78, 083519 4
- Matsubara, T. 2008b, *Physical Review D*, 77 3
- Meiksin, A., White, M. J., & Peacock, J. A. 1999, *Mon. Not. Roy. Astron. Soc.*, 304, 851 2
- Nishimichi, T., et al. 2009, *Publ. Astron. Soc. Jap.*, 61, 321 5
- Noh, Y., White, M., & Padmanabhan, N. 2009, *Physical Review D*, 80 2
- Padmanabhan, N., White, M., & Cohn, J. D. 2009, *Phys. Rev. D*, 79, 063523 2
- Schmittfull, M., Feng, Y., Beutler, F., Sherwin, B., & Chu, M. Y. 2015, *Physical Review D*, 92 2
- Scoccimarro, R., Couchman, H. M. P., & Frieman, J. A. 1999, *Astrophys. J.*, 517, 531 4
- Scoccimarro, R., & Frieman, J. 1996, *Astrophys. J.*, 473, 620 3
- Senatore, L., & Zaldarriaga, M. 2014, arXiv:1409.1225 5
- Seo, H.-J., Beutler, F., Ross, A. J., & Saito, S. 2016, *Mon. Not. Roy. Astron. Soc.*, 460, 2453 2
- Seo, H.-J., Siegel, E. R., Eisenstein, D. J., & White, M. 2008, *Astrophys. J.*, 686, 13 2
- Seo, H.-J., Eckel, J., Eisenstein, D. J., et al. 2010, *Astrophys. J.*, 720, 1650 2
- Sherwin, B. D., & White, M. 2019, *JCAP*, 02, 027 11
- Shirasaki, M., Sugiyama, N. S., Takahashi, R., & Kitaura, F.-S. 2021, *Phys. Rev. D*, 103, 023506 2
- Smith, R. E., Scoccimarro, R., & Sheth, R. K. 2008, *Phys. Rev. D*, 77, 043525 2
- Springel, V. 2005, *Mon. Not. Roy. Astron. Soc.*, 364, 1105 5
- Sugiyama, N. 2024a, *Phys. Rev. D*, 110, 063528 9, 11
- Sugiyama, N. 2024b, arXiv:2403.18262 2, 9, 11
- Sugiyama, N. 2024c, arXiv:2406.01001 2, 4
- Torrado, J., & Lewis, A. 2021, *JCAP*, 05, 057 7
- Wang, Y., et al. 2024a, *Astrophys. J.*, 966, 35 2, 3, 11
- Wang, Y., et al. 2024b, *Commun. Phys.*, 7, 130 2, 11
- White, M. 2015, *Mon. Not. Roy. Astron. Soc.*, 450, 3822 2
- Zang, S.-H., & Zhu, H.-M. 2024, *Astrophys. J.*, 961, 160 2
- Zel'Dovich, Y. B. 1970, *Astronomy and astrophysics*, 5, 84 2, 4
- Zhang, W., Zhao, R., Mu, X., et al. 2025, arXiv:2502.08186 2, 5, 6
- Zhao, R., et al. 2024, *Mon. Not. Roy. Astron. Soc.*, 532, 783 2
- Zhu, H.-M., Yu, Y., & Pen, U.-L. 2018, *Phys. Rev. D*, 97, 043502 2